Gen Relativ Gravit (2015) 47:35
DOI 10.1007/s10714-015-1880-x

RESEARCH ARTICLE

Impact of anisotropic stresses during dissipative gravitational collapse

K. P. Reddy · M. Govender · S. D. Maharaj

Received: 28 July 2014 / Accepted: 26 February 2015 / Published online: 10 March 2015

Abstract We employ a perturbative scheme to study the evolution of a spherically symmetric stellar body undergoing gravitational collapse in the presence of heat dissipation and anisotropic stresses. The Bowers and Liang static model is perturbed, and its subsequent dynamical collapse is studied in the linear perturbative regime. We find that anisotropic effects brought about by the differences in the radial and tangential pressures render the core more unstable than the cooler surface layers. An analysis of the temperature profiles in the interior of the collapsing body shows that the temperature is enhanced in the presence of pressure anisotropy.

Keywords Dissipative collapse · Anisotropic stresses · Causal thermodynamics

1 Introduction

In 1916 Karl Schwarzschild published an exact solution to the Einstein field equations for a spherically symmetric bounded matter distribution having a vacuum exterior. Physically viable models of gravitational collapse became attainable when Vaidya [1] published an exact solution to the field equations describing the exterior gravitational field of a radiating, spherically symmetric mass distribution. Since the star is radiating energy to the exterior spacetime its atmosphere is nonempty and is filled with null

K. P. Reddy · M. Govender (✉) · S. D. Maharaj
Astrophysics and Cosmology Research Unit, School of Mathematics, Statistics and Computer Science, University of KwaZulu-Natal, Private Bag X54001, Durban 4000, South Africa
e-mail: govenderm43@ukzn.ac.za

K. P. Reddy
e-mail: kevinr@dut.ac.za

S. D. Maharaj
e-mail: maharaj@ukzn.ac.za

radiation. The Santos [2] junction conditions obtained by matching the interior spacetime of the collapsing star to Vaidya's outgoing solution paved the way for studying dissipative gravitational collapse.

It became possible to study more realistic scenarios of gravitational collapse which incorporated dissipative fluxes such as heat flow [3,4], shear viscosity [5], bulk viscosity [6] as well as the electromagnetic field [7]. The impact of dissipation on the stability of a gravitationally collapsing stellar fluid has been extensively studied. It is well established that relativistic corrections as a result of heat flow decreases the adiabatic index (which measures the "stiffness" of the collapsing fluid) and renders the fluid less unstable [4,5].

In order to study the thermal behaviour of a star undergoing dissipative gravitational collapse one needs to invoke the transport equations for the relevant dissipative fluxes. To this end, several thermodynamic theories involving irreversible processes have been proposed. The Eckart theory [8] forecasts propagation velocities, for the thermal signals, that lie outside the causal cone of propagation and is additionally plagued with unstable equilibrium states. The "pathological problems" inherent in the Eckart model were addressed, in the context of extended irreversible thermodynamics, by several authors [9–12] by taking into account relaxation time associated with the dissipative fluxes. These models yield hyperbolic transport equations that are of Cattaneo form [13], which obey the causality principle as well as ensuring stable equilibrium states. Di Prisco et al. [14] have estimated the relaxation times for neutron star matter, for early stages of gravitational collapse, to be as small as 0.1 ms for a core temperature of 10^9 K and as large as 100 s at 10^6 K. Work done by Anile et al. [15] also indicate that relaxational effects are significant and Herrera and Martinez [16] show explicitly that thermal relaxation time has a direct impact on the luminosity profiles as well as the compactness of the star.

The effect of the relaxation time on the thermal evolution and luminosity profile of shear-free gravitational collapse has been investigated with the aid of causal transport equations of the Maxwell–Catteneo form for the thermodynamical fluxes [16–20]. Other shear-free models with acceleration and constant (and non-constant) collision time have also been studied in detail [21–23] and they have also found that the star exhibits higher central temperatures when relaxational effects are taken into account. One of the first exact models describing shearing, radiating collapse with pressure anisotropy was presented by Naidu et al. [24]. Their work gives insight into the thermodynamic behaviour of the stellar fluid and the impact of shear on the relaxation time during the collapse process. This model, however, is acceleration-free and results in infinite central pressure and density, and was later generalised by Rajah and Maharaj [25]. Maharaj et al. [26] have explicitly shown how perturbations (in the linear regime) to the temperature profile of a star undergoing shear-free, isotropic dissipative collapse is enhanced (throughout the stellar range) by relaxation effects. Up to that point none of the exact models had a shear-free limit, i.e. the shear could not be switched off, and it was therefore not possible to highlight the effect of shear directly onto the collapse process. A particular collapse model presented by Thirukkanesh et al. [27] has a shear-free limit, ie., the shear can be switched off and the corresponding shear-free collapse ensues. Govender et al. [28] were able to highlight the impact of shear on the temperature and luminosity profiles of this particular model.

The origin and role of anisotropy has been an area of major interest since the early 70's. Superdense stars such as pulsars may be anisotropic for certain density ranges due to phase transitions [29]. Cold matter, above certain high density ranges, may consist of a solid core that is responsible for local anisotropy [30]. Other possible sources of anisotropy are strong electric fields within the star [31], strong magnetic fields [32], the presence of shear [33] and shear viscous pressures [34], amongst numerous other factors. The pioneering work conducted by Bowers and Liang [35] made it possible to study the impact of anisotropy on the physical behaviour (radial pressure, critical mass and maximum surface redshift) of a star undergoing gravitational collapse. By varying the degree of anisotropy, Dev and Gleiser [36] have reported an increase in the critical mass with anisotropy when compared with the mass at the isotropic limit. They also reported a rise in surface redshifts with anisotropy, in particular when the tangential pressure dominates the radial pressure. Investigations [37] and [38] clearly indicate that anisotropy leads to more stable configurations. Herrera [39] found that local pressure anisotropy is one of the factors responsible for energy density inhomogeneities. A recent paper by Sharma and Das [40] gives insight into the impact of the variation of anisotropy on the collapse rate as well as the evolution of the surface temperature of a gravitationally collapsing star with radial heat flux.

In this work we employ the Bowers and Liang static solution as a seed model to investigate the role played by anisotropy for highly dense matter of the order of $10^{15}\,\mathrm{g\,cm^{-3}}$. We employ a linear perturbative scheme to analyse the subsequent dissipative collapse starting off from the initially static Bowers and Liang model. Our investigation centres around the impact of the variation in the anisotropic parameter on the static property variables as well the perturbed quantities, viz. radial and tangential pressures, heat flow, energy density, expansion scalar and temperature profiles. The model allows us to directly measure the behaviour of the above mentioned physical properties starting off with the isotropic case and then seeing the departure from isotropy as the radial pressure gradually begins to dominate the tangential pressure.

The paper is organised as follows: In Sect. 2 we present the field equations describing the geometry and matter content for a star undergoing shearing gravitational collapse. In Sect. 3 we present the perturbative scheme as well as the static and perturbed quantities including the expansion coefficient, shear and mass functions. In Sect. 4 we present the junction conditions for the smooth matching of the interior spacetime with Vaidya's exterior solution across a timelike boundary. In Sect. 5 we present the temporal equation employed in the perturbative scheme that begins with an initially static star that is perturbed so that the perturbations decay exponentially with time. In Sect. 6 we give the results obtained for the static core, and in Sect. 7 we obtain the results for the nonstatic model. In Sect. 8 we study the thermal behaviour of the perturbations by employing a causal heat transport equation. Our results are discussed in Sect. 9.

2 Shearing spacetimes

In this section we follow a similar approach to that of Thirukkanesh et al. [27], Govender et al. [41], Govender et al. [42] and Herrera et al. [43]. The interior spacetime of the

collapsing sphere is described by the general spherically symmetric, shearing metric in comoving coordinates

$$ds^2 = -A^2dt^2 + B^2dr^2 + Y^2(d\theta^2 + \sin^2\theta d\phi^2)\,, \tag{1}$$

where the gravitational potentials $A = A(t, r)$, $B = B(t, r)$ and $Y = Y(t, r)$ are yet to be determined. The matter content for the interior is described (in geometrized units) by

$$T^-_{\alpha\beta} = (\rho + p_t)V_\alpha V_\beta + p_t g_{\alpha\beta} + (p_r - p_t)\chi_\alpha\chi_\beta + q_\alpha V_\beta + q_\beta V_\alpha, \tag{2}$$

where ρ represents the energy density, p_r the radial pressure, p_t the tangential pressure and q^α the heat flux vector. The fluid four-velocity (V^α), radial unit four-vector (χ^α) and the heat flux (q^α) must satisfy the following conditions:

$$V_\alpha V^\alpha = -1, \quad \chi^\alpha\chi_\alpha = 1, \quad \chi^\alpha V_\alpha = 0, \quad V_\alpha q^\alpha = 0. \tag{3}$$

The collapse rate and the fluid four-acceleration are given by

$$\Theta = V^\alpha{}_{;\alpha}, \quad a_\alpha = V_{\alpha;\beta}V^\beta, \tag{4}$$

and the shear tensor σ_{α_β} by

$$\sigma_{\alpha_\beta} = V_{(\alpha;\beta)} + a_{(\alpha}V_{\beta)} - \frac{1}{3}\Theta(g_{\alpha\beta} + V_\alpha V_\beta). \tag{5}$$

For the comoving line element (1), the fluid four-velocity (V^α) and the radial unit four-vector (χ^α) are given respectively by:

$$V^\alpha = A^{-1}\delta^\alpha_0, \quad \chi^\alpha = B^{-1}\delta^\alpha_1. \tag{6}$$

The heat flow vector q^α takes on the form

$$q^\alpha = (0, q_1, 0, 0) \tag{7}$$

since $V_\alpha q^\alpha = 0$ ensures radial heat flow. Using (4) with (6) yields the four-acceleration and its magnitude (scalar) in the form

$$a_1 = \frac{A'}{A}, \quad a^\alpha a_\alpha = \left(\frac{A'}{AB}\right)^2, \tag{8}$$

and for the collapse rate we get

$$\Theta = \frac{1}{A}\left(\frac{\dot{B}}{B} + 2\frac{\dot{Y}}{Y}\right), \tag{9}$$

where dots and primes denote differentiation with respect to t and r respectively. With the aid of (5) and (6) we obtain the following nonzero components for the shear

$$\sigma_{11} = \frac{2}{3}B^2\sigma, \quad \sigma_{22} = \sigma_{33}\sin^{-2}\theta = -\frac{1}{3}Y^2\sigma, \tag{10}$$

where

$$\sigma = \frac{1}{A}\left(\frac{\dot{B}}{B} - \frac{\dot{Y}}{Y}\right), \tag{11}$$

and the shear scalar is of the form

$$\sigma^{\alpha\beta}\sigma_{\alpha\beta} = \frac{2}{3}\sigma^2. \tag{12}$$

By employing geometrized units (wherein the speed of light c, and the coupling coefficient $8\pi G/c^4$ are taken to be unity), the nonzero components of the Einstein field equations, for the line element (1) and the energy momentum (2), are

$$G_{00}^{-} = T_{00}^{-} = \rho A^2 = \left(2\frac{\dot{B}}{B} + \frac{\dot{Y}}{Y}\right)\frac{\dot{Y}}{Y} - \left(\frac{A}{B}\right)^2\left[2\frac{Y''}{Y} + \left(\frac{Y'}{Y}\right)^2 - 2\frac{B'}{B}\frac{Y'}{Y} - \left(\frac{B}{Y}\right)^2\right], \tag{13}$$

$$G_{11}^{-} = T_{11}^{-} = p_r B^2 = -\left(\frac{B}{A}\right)^2\left[2\frac{\ddot{Y}}{Y} - \left(2\frac{\dot{A}}{A} - \frac{\dot{Y}}{Y}\right)\frac{\dot{Y}}{Y}\right] + \frac{Y'}{Y}\left(2\frac{A'}{A} + \frac{Y'}{Y}\right) - \frac{B^2}{Y^2}, \tag{14}$$

$$G_{22}^{-} = T_{22}^{-} = p_t Y^2 = -\left(\frac{Y}{A}\right)^2\left[\frac{\ddot{B}}{B} + \frac{\ddot{Y}}{Y} - \frac{\dot{A}}{A}\left(\frac{\dot{B}}{B} + \frac{\dot{Y}}{Y}\right) + \frac{\dot{B}}{B}\frac{\dot{Y}}{Y}\right] + \left(\frac{Y}{B}\right)^2\left[\frac{A''}{A} + \frac{Y''}{Y} - \frac{A'}{A}\frac{B'}{B} + \left(\frac{A'}{A} - \frac{B'}{B}\right)\frac{Y'}{Y}\right], \tag{15}$$

$$G_{01}^{-} = T_{01}^{-} = q_1 AB^2 = -2\left(-\frac{\dot{Y}'}{Y} + \frac{\dot{B}}{B}\frac{Y'}{Y} + \frac{\dot{Y}}{Y}\frac{A'}{A}\right). \tag{16}$$

This is an underdetermined system of four coupled partial differential equations in seven unknowns, viz. A, B, Y, ρ, p_r, p_t and q_1. Note that q_1 is related to the radially directed heat flow vector whose magnitude Q is given by

$$Q = (q_\alpha q^\alpha)^{\frac{1}{2}} = q_1 B. \tag{17}$$

Also note that (16) can be re-written using (9) and (11) as follows

$$q_1 B = \frac{1}{B}\left[\frac{2}{3}(\Theta - \sigma)' - \frac{2Y'\sigma}{Y}\right]. \tag{18}$$

The mass function $m(t, r)$ is given by

$$m(t, r) = \frac{Y}{2}\left[\left(\frac{\dot{Y}}{Y}\right)^2 - \left(\frac{Y'}{B}\right)^2 + 1\right]. \tag{19}$$

3 Perturbative scheme

The perturbative scheme used in this study has been used by several authors [4,5,44] and [45] We assume an initially static fluid described by quantities having only radial dependence. Such quantities are denoted using the subscript zero. We also suppose that the metric function $A(t, r)$, $B(t, r)$ and $Y(t, r)$ and their perturbations have the same time dependence. For mathematical convenience, we assume that the metric and material functions are given by

$$A(t, r) = A_o(r) + \lambda T(t)a(r), \tag{20}$$
$$B(t, r) = B_o(r) + \lambda T(t)b(r), \tag{21}$$
$$Y(t, r) = Y_o(r) + \lambda T(t)y(r), \tag{22}$$
$$\rho(t, r) = \rho_o(r) + \lambda\overline{\rho}(t, r), \tag{23}$$
$$p_r(t, r) = p_{ro}(r) + \lambda\overline{p_r}(t, r), \tag{24}$$
$$p_t(t, r) = p_{to}(r) + \lambda\overline{p_t}(t, r), \tag{25}$$
$$m(t, r) = m_o(r) + \lambda\overline{m}(t, r), \tag{26}$$
$$\Theta(t, r) = \lambda\overline{\Theta}(t, r), \tag{27}$$
$$\sigma(t, r) = \lambda\overline{\sigma}(t, r), \tag{28}$$
$$q_1(t, r) = \lambda\overline{q}_1(t, r), \tag{29}$$

where $0 < \lambda \ll 1$ is the perturbation amplitude and quantities with an 'over bar' represent perturbed quantities. We should point out that if one starts from spherical symmetry alone, one indeed has a very large gauge (coordinate) freedom to write the line element. However, once the line element is assumed as given by (1), all coordinate freedom is exhausted leaving only the possibility of rescaling the radial coordinate r and/or the time-like coordinate t. As it is evident by simple inspection, such rescaling would not change the form of Eqs. (20)–(29). In essence, the choice of the perturbed variables as given in (20)–(29) is not unique. However, once the line element is prescribed, the choice of the perturbed variables cannot be changed to produce the same physical results. The shear-free case within this perturbative scheme was studied by several authors [4,5] and [44]. In all these investigations the

static model was taken to be the isotropic Schwarzschild interior solution. Taking into consideration (20)–(29), we obtain the relationships for the static configuration:

$$\rho_o = -\frac{1}{B_o^2}\left(\frac{2Y_o''}{Y_o} + \frac{Y_o'^2}{Y_o^2} - \frac{2Y_o'B_o'}{Y_oB_o} - \frac{B_o^2}{Y_o^2}\right), \tag{30}$$

$$p_{ro} = \frac{1}{B_o^2}\left(\frac{2A_o'Y_o'}{A_oY_o} + \frac{Y_o'^2}{Y_o^2} - \frac{B_o^2}{Y_o^2}\right), \tag{31}$$

$$p_{to} = \frac{1}{B_o^2}\left[\frac{A_o''}{A_o} + \frac{Y_o''}{Y_o} - \frac{A_o'B_o'}{A_oB_o} + \frac{Y_o'}{Y_o}\left(\frac{A_o'}{A_o} - \frac{B_o'}{B_o}\right)\right], \tag{32}$$

and from (13) to (16) we obtain the perturbed quantities

$$\overline{\rho} = -\frac{2bT\rho_o}{B_o} - \frac{2T}{{B_o}^2}\left[\left(\frac{y}{Y_o}\right)'' - \frac{1}{Y_o}\left(\frac{b}{B_o}\right)' - \left(\frac{B_o'}{B_o} - \frac{3}{Y_o}\right)\left(\frac{y}{Y_o}\right)' - \left(\frac{B_o}{Y_o}\right)^2\left(\frac{b}{B_o} - \frac{y}{Y_o}\right)\right], \tag{33}$$

$$\overline{p}_r = -\frac{2p_{ro}bT}{B_o} - \frac{2\ddot{T}y}{A_o^2Y_o} + \frac{2T}{Y_oB_o^2}\left[Y_o'\left(\frac{a}{A_o}\right)' + \left(\frac{y}{Y_o}\right)'\left(Y_o' + \frac{A_o'Y_o}{A_o}\right) - \frac{B_o^2}{Y_o}\left(\frac{b}{B_o} - \frac{y}{Y_o}\right)\right], \tag{34}$$

$$\overline{p}_t = -\frac{2bTp_{to}}{B_o} - \frac{\ddot{T}}{A_o^2}\left(\frac{b}{B_o} + \frac{y}{Y_o}\right) + \frac{T}{B_o^2}\left[\left(\frac{y}{Y_o}\right)'' + \left(\frac{a}{A_o}\right)'' + \left(\frac{2A_o'}{A_o} - \frac{B_o'}{B_o} + \frac{Y_o'}{Y_o}\right)\left(\frac{a}{A_o}\right)' - \left(\frac{A_o'}{A_o} + \frac{Y_o'}{Y_o}\right)\left(\frac{b}{B_o}\right)' + \left(\frac{A_o'}{A_o} - \frac{B_o'}{B_o} + \frac{2Y_o'}{Y_o}\right)\left(\frac{y}{Y_o}\right)'\right], \tag{35}$$

$$\overline{q}_1B_o = -\frac{2\dot{T}}{A_oB_o}\left[\frac{bY_o'}{B_oY_o} + \frac{y}{Y_o}\left(\frac{A_o'}{A_o} - \frac{Y_o'}{Y_o}\right) - \left(\frac{y}{Y_o}\right)'\right]. \tag{36}$$

These equations generalize the recent work by Herrera et al. [46] in which they considered a similar perturbative scheme with vanishing heat flux. Expressions for the perturbed expansion coefficient and shear are given respectively by

$$\overline{\Theta} = \frac{\dot{T}}{A_o}\left(\frac{b}{B_o} + 2\frac{y}{Y_o}\right), \tag{37}$$

and

$$\overline{\sigma} = \frac{\dot{T}}{A_o}\left(\frac{b}{B_o} - \frac{y}{Y_o}\right). \tag{38}$$

The static and perturbed configuration for the mass function are respectively

$$m_o = \frac{Y_o}{2}\left[1 - \left(\frac{Y_o'}{B_o}\right)^2\right], \tag{39}$$

and

$$\overline{m} = -\frac{T}{B_o^2}\left[Y_o\left(Y_o' y' - \frac{{Y_o'}^2 b}{B_o}\right) + \frac{y}{2}\left({Y_o'}^2 - {B_o}^2\right)\right]. \tag{40}$$

4 Exterior spacetime and junction conditions

The exterior spacetime is taken to be the Vaidya solution given by [1]

$$ds^2 = -\left(1 - \frac{2m(v)}{\Re}\right)dv^2 - 2dvd\Re + \Re^2\left(d\theta^2 + \sin^2\theta d\phi^2\right), \tag{41}$$

in the coordinates $x^i = (v, \Re, \theta, \phi)$ where $m(v)$ represents the Newtonian mass of the gravitating body as measured by an observer at infinity. The necessary conditions for the smooth matching of the interior spacetime (1) to the exterior spacetime (41) have been extensively investigated. We present the main results that are necessary for modeling a radiating star. The continuity of the intrinsic and extrinsic curvature components of the interior and exterior spacetimes across a timelike boundary are

$$A\left(r_\Sigma, t\right)dt = \left(1 - \frac{2m(v)}{\Re_\Sigma} + 2\frac{d\Re_\Sigma}{dv}\right)^{\frac{1}{2}} dv, \tag{42}$$

$$Y(r_\Sigma, t) = \Re_\Sigma(v), \tag{43}$$

$$m(v)_\Sigma = \left\{\frac{Y}{2}\left[\left(\frac{\dot{Y}}{A}\right)^2 - \left(\frac{Y'}{B}\right)^2 + 1\right]\right\}_\Sigma, \tag{44}$$

$$(p_r)_\Sigma = (q_1 B)_\Sigma. \tag{45}$$

Equation (44) represents the total gravitational mass that is contained within the boundary (Σ) of the star. Equation (45) clearly shows that the radial pressure at the boundary of a star undergoing dissipative collapse is equal to the magnitude of the heat flow. The radial pressure at the boundary vanishes when the heat flow at the boundary is zero.

5 The temporal equation employed in the perturbation scheme

Relation (45) together with (36) and $(p_{ro})_\Sigma = 0$ in (34) determines the temporal evolution of the collapsing star, and is given by

$$\alpha_\Sigma T - \ddot{T} = 2\beta_\Sigma \dot{T} > 0, \tag{46}$$

where

$$\alpha_\Sigma = \left\{ \frac{A_o^2}{B_o^2 y}\left[Y_o' \left(\frac{a}{A_o}\right)' + \left(\frac{y}{Y_o}\right)' \left(Y_o' + \frac{A_o' Y_o}{A_o}\right) - \frac{B_o^2}{Y_o}\left(\frac{b}{B_o} - \frac{y}{Y_o}\right)\right]\right\}_\Sigma , \tag{47}$$

and

$$\beta_\Sigma = \left\{ -\frac{A_o Y_o}{2B_o y}\left[\frac{bY_o'}{B_o Y_o} + \frac{y}{Y_o}\left(\frac{A_o'}{A_o} - \frac{Y_o'}{Y_o}\right) - \left(\frac{y}{Y_o}\right)'\right]\right\}_\Sigma . \tag{48}$$

Solutions of (46) include exponential functions (growth and decay) as well as oscillatory functions. In order to model collapse we will consider an exponential decaying function which represents an initially static system at $t = -\infty$, ie. $T(-\infty) = 0$ with a decreasing luminosity radius as t increases. This temporal behaviour of our model is fulfilled if $\alpha_\Sigma > 0$ and $\beta \leq 0$. The temporal evolution of our model is then given by

$$T(t) = -e^{\left(-\beta_\Sigma + \sqrt{\alpha_\Sigma + \beta_\Sigma{}^2}\right)t}, \tag{49}$$

With the aid of (48), Eq. (36) can be expressed as

$$\overline{q}_1 B_o = \frac{4y\beta}{A_o^2 Y_o}\dot{T}. \tag{50}$$

where $\beta = \beta(r)$. Note that when $\beta_\Sigma = 0$ (ie., no dissipation), the system continues to collapse.

6 The static core

We take the interior static solution to be the Bowers and Liang [35] model with constant density. This model is the generalisation of the interior Schwarzschild solution to include anisotropic pressures. The Bowers and Liang model has been used extensively to investigate the role played by local anisotropy in highly dense matter distributions typically of the order of 10^{15} g cm^{-3}. If we denote the fractional anisotropy by $\Delta_f = \frac{p_t - p_r}{p_r}$ then the Bowers and Liang model exhibits the following features:

(a) $\Delta_f > 0$: The maximum equilibrium mass and surface redshift are greater than their corresponding isotropic ($\Delta_f = 0$) counterparts.
(b) $\Delta_f < 0$: The maximum mass and surface redshift are less than their corresponding isotropic values.

Moreover, the anisotropy allows for arbitrarily large surface redshifts as observed in quasars.

The line element for the Bowers and Liang solution is

$$ds^2 = -\left[\frac{3\left(1-2M/r_\Sigma\right)^{h/2} - \left(1-2m/r\right)^{h/2}}{2}\right]^{2/h} dt^2 + \left(1-\frac{2m}{r}\right)^{-1} dr^2 + r^2\left(d\theta^2 + \sin^2\theta d\phi^2\right), \tag{51}$$

where h is a constant and $0 \le r \le R$. From the metric (51) it is clear that

$$A_o^2 = \left[\frac{3\left(1-2M/r_\Sigma\right)^{h/2} - \left(1-2m/r\right)^{h/2}}{2}\right]^{2/h}, \tag{52}$$

$$B_o^2 = \left(1-\frac{2m}{r}\right)^{-1}, \tag{53}$$

and

$$Y_o = r. \tag{54}$$

In the physical analysis that follows we take

$$a = -k_1(r+1)^{-1}, \quad b = k_2(r+1)^{-1}, \quad y = k_3, \quad m = \frac{r^3 M}{R^3}, \tag{55}$$

where $k_1 = k_2 = 10^{-17}$ and $k_3 = 10^{-1}$. Using (52)–(55), Eqs. (30)–(32) become, respectively,

$$\rho_o = 6M/R^3, \tag{56}$$

$$p_{ro} = \left(1-\frac{2Mr^2}{R^3}\right)\left[\frac{4M\left(1-\frac{2Mr^2}{R^3}\right)^{\frac{h}{2}-1}}{R^3\left(3\left(1-\frac{2M}{R}\right)^{h/2} - \left(1-\frac{2Mr^2}{R^3}\right)^{h/2}\right)} - \frac{1}{r^2\left(1-\frac{2Mr^2}{R^3}\right)} + \frac{1}{r^2}\right] \tag{57}$$

$$p_{to} = \left[6M\left(2Mr^2\left(-h\left(1-\frac{2M}{R}\right)^{h/2}\left(1-\frac{2Mr^2}{R^3}\right)^{h/2} - 3\left(1-\frac{2M}{R}\right)^{h/2} \times \left(1-\frac{2Mr^2}{R^3}\right)^{h/2} + \left(1-\frac{2Mr^2}{R^3}\right)^{h} + 3\left(1-\frac{2M}{R}\right)^{h}\right) - R^3\left(-4\left(1-\frac{2M}{R}\right)^{h/2}\left(1-\frac{2Mr^2}{R^3}\right)^{h/2} + \left(1-\frac{2Mr^2}{R^3}\right)^{h}\right)\right.$$

$$+3\left(1-\frac{2M}{R}\right)^{h}\Big)\Big)\Big]\times\Big[R^3\left(R^3-2Mr^2\right)\Big(\Big(1-\frac{2Mr^2}{R^3}\Big)^{h/2}$$
$$-3\left(1-\frac{2M}{R}\right)^{h/2}\Big)^2\Big]^{-1} \tag{58}$$

The anisotropy parameter $\Delta = p_t - p_r$ is expressed (for the static case) as

$$\Delta = -\frac{12(h-1)M^2r^2\left(1-\frac{2M}{R}\right)^{h/2}\left(1-\frac{2Mr^2}{R^3}\right)^{h/2}}{R^3\left(R^3-2Mr^2\right)\left(\left(1-\frac{2Mr^2}{R^3}\right)^{h/2}-3\left(1-\frac{2M}{R}\right)^{h/2}\right)^2} \tag{59}$$

We point out that Eqs. (60)–(66) below, including their derivation, can be found in a review article by Herrera and Santos [33]. We simply state the equations here and discuss the relationship between the order parameter Δ and the anisotropic factor C. Δ can also be written as

$$\Delta = \frac{4}{3}\pi Cr^2\Big(\rho_o + p_{ro}\Big)\Big(\rho_o + 3p_{ro}\Big)\Big(1-\frac{2m}{r}\Big)^{-1} \tag{60}$$

where C, the anisotropic factor, measures the degree of anisotropy and is given by

$$h = 1 - 2C. \tag{61}$$

It follows from Eq. (60) that the anisotropic parameter can be recast as $\Delta = C\chi(r)$, where $\chi(r) = \frac{4}{3}\pi r^2\big(\rho_o+p_{ro}\big)\big(\rho_o+3p_{ro}\big)\big(1-\frac{2m}{r}\big)^{-1}$. We also point out that $\chi(r) > 0$ for all r, implying that Δ is directly proportional (and of similar sign) to C. From (61) it is clear that $h = 1$ corresponds to $C = 0$ which is the isotropic case, while $h = 2$ and $h = 4$ correspond respectively to $C = -\frac{1}{2}$ and $C = -\frac{3}{2}$ which imply that the radial pressure dominates the tangential pressure. The model has a limiting case of $h = 0$ which corresponds to the Florides [47] solution which is not considered in our analysis.

The critical value of $2M/r_\Sigma$ resulting in infinite central pressure is given by

$$\left(\frac{2M}{r_\Sigma}\right)_{crit} = 1-\left(\frac{1}{3}\right)^{2/h}, \tag{62}$$

and the associated critical mass is given by

$$M_{crit} = \left(\frac{3}{32\pi\rho_o}\right)^{1/2}\left[1-\left(\frac{1}{3}\right)^{2/h}\right]^{3/2}. \tag{63}$$

It is also worthwhile to note that the ratio of the anisotropic critical mass to that of the isotropic case is given by

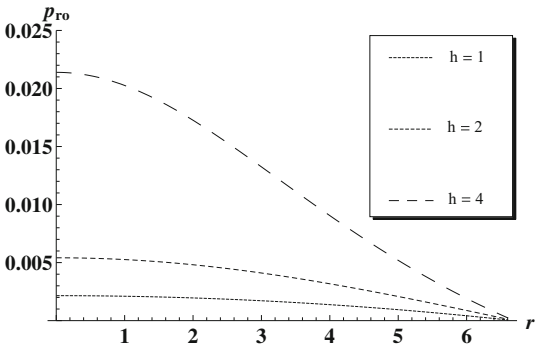

Fig. 1 Static radial pressure p_{ro} profiles versus radial coordinate for $M = 1$ and $R = 6.6$

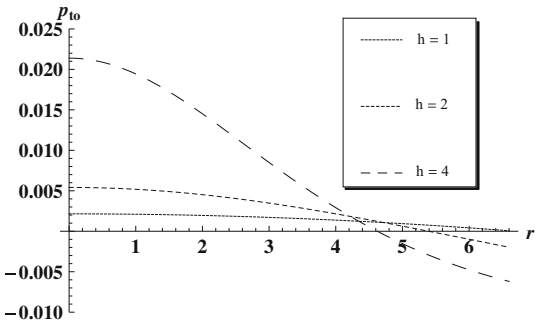

Fig. 2 Static tangential pressure p_{to} profiles versus radial coordinate for $M = 1$ and $R = 6.6$

$$\frac{(M_{ani})_{crit}}{(M_{iso})_{crit}} = \frac{8}{9}\left[1 - \left(\frac{1}{3}\right)^{2/h}\right]^{3/2}. \tag{64}$$

The redshift z at the star's surface is expressed as

$$z = \left(1 - \frac{2M}{r_\Sigma}\right)^{-1/2} - 1. \tag{65}$$

Using Eq. (65), the critical value of the red shift is

$$z_{crit} = 3^{1/h} - 1. \tag{66}$$

From Fig. 1 we note that static radial pressure is a monotonically decreasing function of the radial coordinate r. In addition, the radial pressure is enhanced at each interior point of the stellar distribution as the relative anisotropy increases (larger h values). Figure 2 shows a peculiar trend in the tangential pressure within the stellar core. We observe that p_{to} is positive and decreases monotonically from the center until it vanishes at some radius $r = r_1 < R$ and becomes negative as one moves towards the stellar surface. The effect of a positive tangential pressure is to 'squeeze' each concentric shell of the stellar fluid. For the region $0 \leq r \leq r_1$, the positive tangential pressure decreases and the effect of this is to have a fluid configuration with more

relaxed shells as one moves away from the centre towards r_1. Equilibrium in this region is achieved by a balance between the outward radial pressure and the sum of the inward gravitational force and the squeezing of the shells due to the positive tangential pressure. At $r = r_1$ the tangential pressure vanishes and equilibrium is achieved by the balance between the radial pressure and gravity. In the region $r_1 \leq r \leq R$, the negative tangential pressure has the tendency to 'expand' each concentric shell of the stellar fluid. This effect combines with the radial pressure to balance the inwardly directed gravitational force to produce equilibrium. The variation in the tangential pressure throughout the stellar interior can be brought out by various physical processes such as exotic phase transitions, neutrino-trapping, variation of the equation of state amongst other mechanisms [33]. It is clear from Fig. 2, that anisotropy enhances the behaviour of the tangential pressure within the stellar interior.

7 The nonstatic model

Using Eqs. (33)–(38) we obtain the perturbation in the density, radial pressure, tangential pressure, heat flow, collapse rate and shear respectively. These have the forms

$$\begin{aligned}\overline{\rho} &= 2T(t)\Bigg(k_2\left(2Mr^2-R^3\right)\left(2Mr^2+r^2(r+1)R^3\rho_o-R^3\right)-4k_3Mr\\ &\quad\times(r+1)^2R^3\sqrt{1-\frac{2Mr^2}{R^3}}\Bigg)\left(r^2(r+1)^2R^6\sqrt{1-\frac{2Mr^2}{R^3}}\right)^{-1}, \qquad (67)\\ \overline{p}_r &= \frac{12k_2MT(t)\sqrt{1-\frac{2Mr^2}{R^3}}\left(\left(1-\frac{2Mr^2}{R^3}\right)^{h/2}-\left(1-\frac{2M}{R}\right)^{h/2}\right)}{(r+1)R^3\left(\left(1-\frac{2Mr^2}{R^3}\right)^{h/2}-3\left(1-\frac{2M}{R}\right)^{h/2}\right)}\\ &\quad+\frac{1}{2Mr^3-rR^3}2\left(1-\frac{2Mr^2}{R^3}\right)T(t)\Bigg[-(r+1)^{-2}2^{\frac{1}{h}}\left(3\left(1-\frac{2M}{R}\right)^{h/2}\right.\\ &\quad\left.-\left(1-\frac{2Mr^2}{R^3}\right)^{h/2}\right)^{-\frac{h+1}{h}}\Bigg[\left(2Mr(2r+1)-R^3\right)\left(1-\frac{2Mr^2}{R^3}\right)^{h/2}\\ &\quad+3\left(1-\frac{2M}{R}\right)^{h/2}\left(R^3-2Mr^2\right)\Bigg]k_1+k_2R^3\sqrt{1-\frac{2Mr^2}{R^3}}(r(r+1))^{-1}\\ &\quad+2MT(t)k_3\left(\frac{1}{3\left(1-\frac{2M}{R}\right)^{h/2}\left(1-\frac{2Mr^2}{R^3}\right)^{-h/2}-1}-1\right)\Bigg]\\ &\quad-2^{\frac{h+2}{h}}k_3\dot{T}(t)\left(3\left(1-\frac{2M}{R}\right)^{h/2}-\left(1-\frac{2Mr^2}{R^3}\right)^{h/2}\right)^{-2/h}r^{-1}, \qquad (68)\end{aligned}$$

$$\overline{q}_1 B_o = 2^{\frac{1}{h}+1} T'(t) \left(3 \left(1 - \frac{2M}{R} \right)^{h/2} - \left(1 - \frac{2Mr^2}{R^3} \right)^{h/2} \right)^{-\frac{h+1}{h}}$$
$$\times \left(2k_3 Mr(r+1) \left(1 - \frac{2Mr^2}{R^3} \right)^{\frac{h+1}{2}} - k_2 \left(R^3 - 2Mr^2 \right)^2 \right.$$
$$\times \left[\left(1 - \frac{2Mr^2}{R^3} \right)^{h/2} - 3 \left(1 - \frac{2M}{R} \right)^{h/2} \right] R^{-3} \Big)$$
$$\left. \times \left(r(r+1) \left(2Mr^2 - R^3 \right) \right) \right)^{-1} \tag{69}$$

$$\overline{\Theta} = 2^{\frac{1}{h}} \dot{T}(t) \left(3 \left(1 - \frac{2M}{R} \right)^{h/2} - \left(1 - \frac{2Mr^2}{R^3} \right)^{h/2} \right)^{-1/h}$$
$$\times \left(\frac{k_2 \sqrt{1 - \frac{2Mr^2}{R^3}}}{r+1} + \frac{2k_3}{r} \right) \tag{70}$$

$$\overline{\sigma} = 2^{\frac{1}{h}} \dot{T}(t) \left(3 \left(1 - \frac{2M}{R} \right)^{h/2} - \left(1 - \frac{2Mr^2}{R^3} \right)^{h/2} \right)^{-1/h}$$
$$\times \left(\frac{k_2 \sqrt{1 - \frac{2Mr^2}{R^3}}}{r+1} - \frac{k_3}{r} \right) \tag{71}$$

where $T(t)$ is given by (49). We note from (7) that the perturbed density does not depend on the anisotropic factor h. We also note that the expression for the perturbed tangential pressure $\overline{p}_t$ has not been included here due to its length and complexity. From Fig. 3 (late time collapse) and Fig. 4 (early time collapse) we observe that the perturbations in the energy density are positive at each interior point of the core and gradually decrease as one approaches the stellar surface. Figures 5 and 6 illustrate the evolution of the central and surface perturbations of the density as functions of time. As expected, the perturbations increase as the collapse proceeds. It is important to

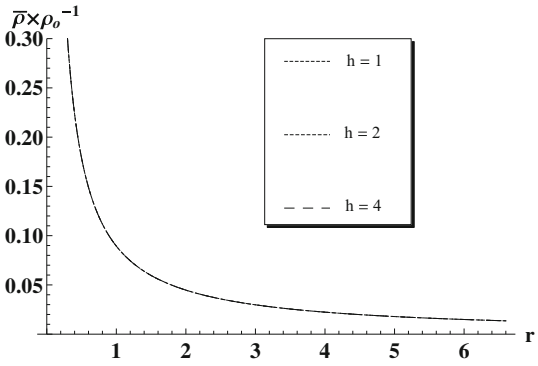

Fig. 3 Profiles of the ratio of the perturbed energy density $\overline{\rho}$ to the static energy ρ_o for late time collapse versus radial the coordinate ($M = 1$, $R = 6.6$, $\rho_o = 0.02$ and $t = -1$)

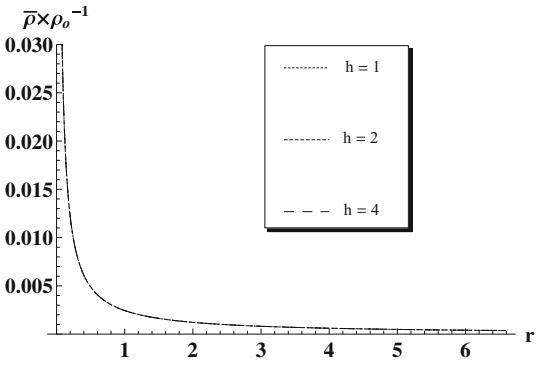

Fig. 4 Profiles of the ratio of the perturbed energy density $\overline{\rho}$ to the static energy ρ_o for early time collapse versus the radial coordinate ($M = 1$, $R = 6.6$, $\rho_o = 0.02$ and $t = -10$)

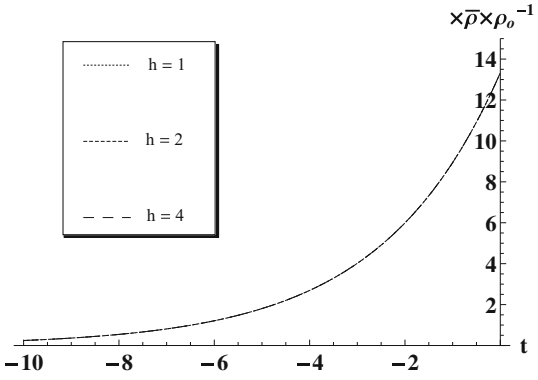

Fig. 5 Profiles of the ratio of the perturbed energy density $\overline{\rho}$ to the static energy ρ_o near the centre versus the time coordinate ($M = 1$, $R = 6.6$, $\rho_o = 0.02$ and $r = 0.01$)

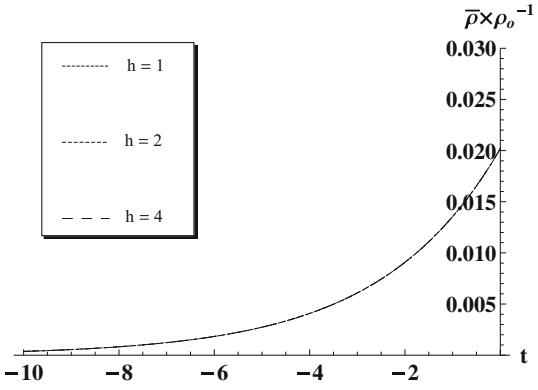

Fig. 6 Profiles of the ratio of the perturbed energy density $\overline{\rho}$ to the static energy ρ_o near the surface versus the time coordinate ($M = 1$, $R = 6.6$, $\rho_o = 0.02$ and $r = 6.6$)

note that anisotropy plays no significant role in the evolution of the perturbations in the energy density.

Figures 7 and 8 display the perturbations to the radial pressure as a function of the radial coordinate for late time and early time collapse respectively. We observe that the perturbations in the energy density and radial pressure are both positive which lead to an overall increase in the energy density and radial pressure within the collapsing

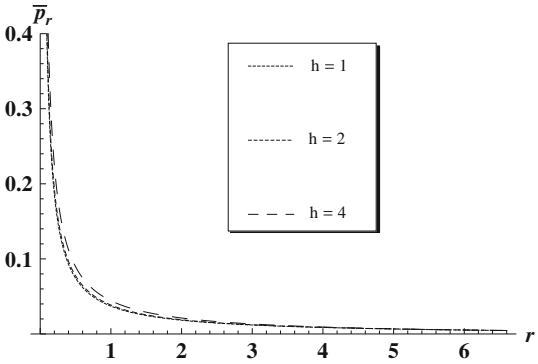

Fig. 7 Profiles of perturbed radial pressure $\overline{p}_r$ versus radial coordinate for late time collapse ($M = 1$, $R = 6.6$ and $t = -1$)

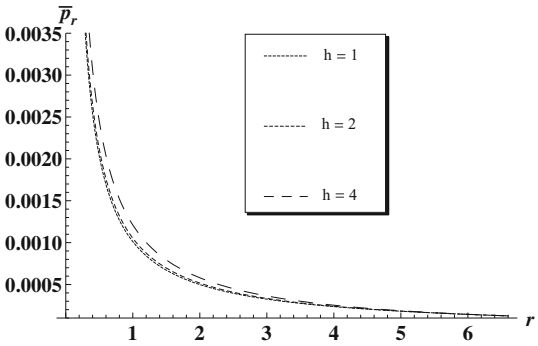

Fig. 8 Profiles of perturbed radial pressure $\overline{p}_r$ versus radial coordinate for early time collapse ($M = 1$, $R = 6.6$ and $t = -10$)

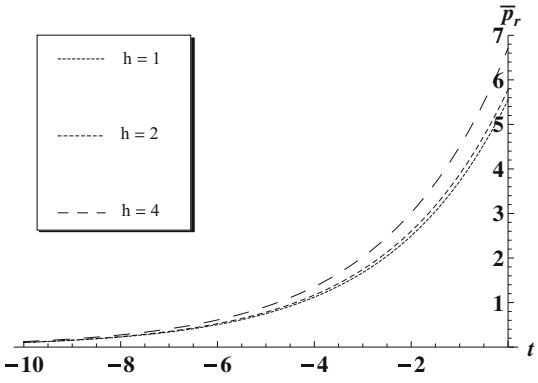

Fig. 9 Profiles of perturbed radial pressure $\overline{p}_r$ versus time coordinate near the centre of the star ($M = 1$, $R = 6.6$ and $r = 0.01$)

star. Furthermore, it is evident that the perturbations in the radial pressure increase with increasing anisotropy (larger h). Figures 9 and 10 display the temporal evolution of the radial pressure near the centre and and at the surface of the star respectively. It is evident from Fig.10 that anisotropic effects are enhanced in the central regions of the collapsing body for late times of the collapse period.

Figures 11 and 12 show the perturbations in the tangential pressure for late times and early times collapse respectively. It is interesting to note that anisotropy 'drives'

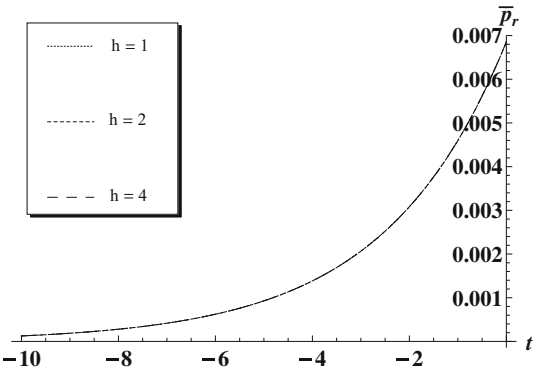

Fig. 10 Profiles of perturbed radial pressure $\overline{p}_r$ versus time coordinate near the surface of the star ($M = 1$, $R = 6.6$ and $r = 6.6$)

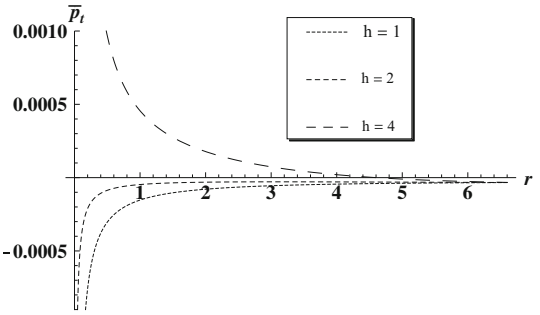

Fig. 11 profiles of perturbed tangential pressure $\overline{p}_t$ versus radial coordinate for late time collapse ($M = 1$, $R = 6.6$ and $t = -1$)

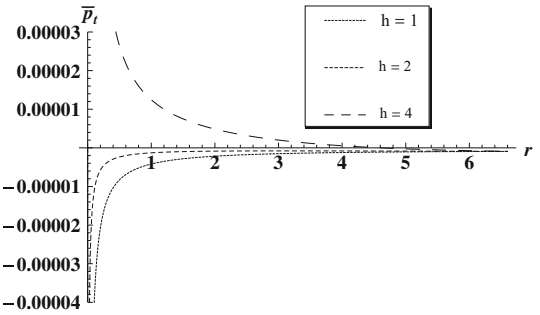

Fig. 12 profiles of perturbed tangential pressure $\overline{p}_t$ versus radial coordinate for early time collapse ($M = 1$, $R = 6.6$ and $t = -10$)

the perturbations to become positive. This implies that the total tangential pressure increases with an increase in anisotropy rendering the core more unstable, particularly in the central regions.

Figures 13 and 14 display the behaviour of the heat flux as a function of the radial coordinate for late time and early time collapse respectively. We observe that the heat flux is maximum at the centre where the pressure is the highest, and then gradually drops off towards the surface. Heat generation is enhanced in the central regions of the collapsing star as the anisotropy increases. Figures 15 and 16 display the variation of the heat flux near the centre and at the surface respectively as a function of time. We observe that the heat flux is maximum at the centre where the pressure is the highest,

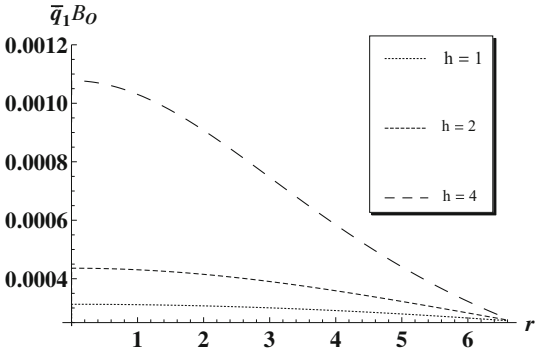

Fig. 13 Profiles of the perturbed heat flow $\overline{q}_1 B_o$ for late time collapse versus radial coordinate ($M = 1$, $R = 6.6$ and $t = -1$)

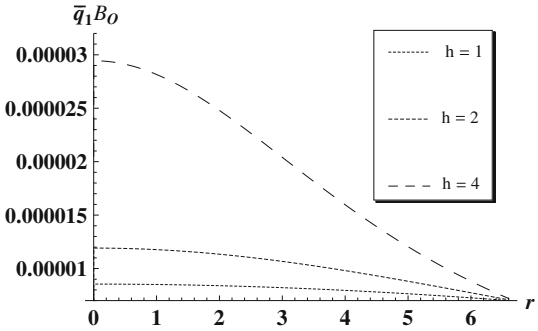

Fig. 14 Profiles of the perturbed heat flow $\overline{q}_1 B_o$ for early time collapse versus radial coordinate ($M = 1$, $R = 6.6$ and $t = -10$)

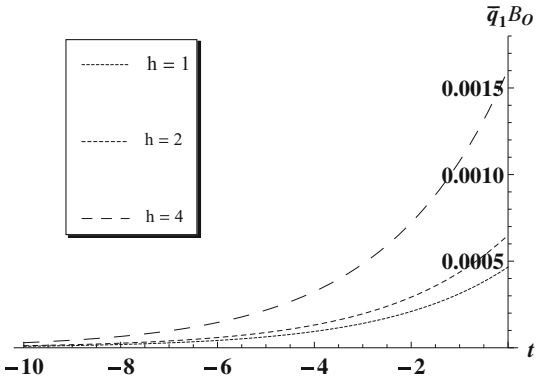

Fig. 15 Profiles of the perturbed heat flow $\overline{q}_1 B_o$ versus time coordinate near the centre of the star ($M = 1$, $R = 6.6$ and $r = 0.01$)

and then gradually drops off towards the surface. Heat generation is enhanced in the central regions of the collapsing star as the anisotropy increases.

Figures 17 and 18 illustrate the collapse rate for late time and early time collapse as a function of the radial coordinate respectively. We clearly see a deviation from isotropy closer to the central regions of the collapsing core. In Fig. 19 we plotted the ratio of the collapse rate at the centre to the collapse rate at the surface as a function of time. The collapse rate at the centre is higher than the collapse rate at the cooler surface layers. Furthermore, this ratio increases with an increase in pressure anisotropy. The

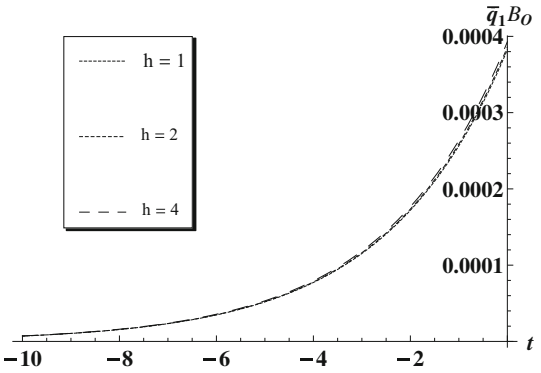

Fig. 16 Profiles of the perturbed heat flow $\overline{q}_1 B_o$ versus time coordinate near the surface of the star ($M = 1$, $R = 6.6$ and $r = 6.6$)

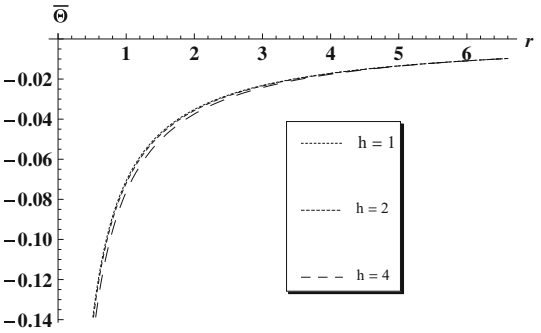

Fig. 17 Profiles of the collapse for late time collapse versus radial coordinate ($M = 1$, $t = -1$ and $R = 6.6$)

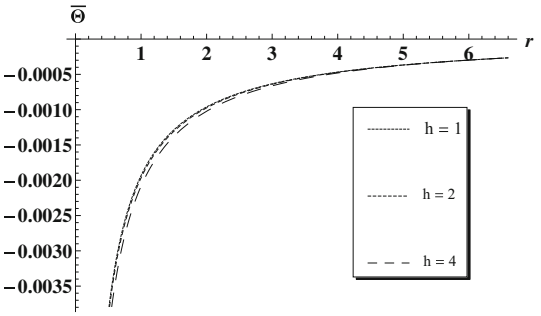

Fig. 18 Profiles of the collapse for early time collapse versus radial coordinate ($M = 1$, $t = -10$ and $R = 6.6$)

heat generation coupled with the anisotropy in the pressure leads to more unstable central regions resulting in nonhomogeneous collapse.

Figures 20 and 21 display the perturbations in the shear at the centre and surface as functions of time respectively. We observe that shearing effects dominate closer to the centre of the collapsing body and the effect of pressure anisotropy becomes more pronounced in this region for late times. Figures 22 and 23 show the perturbations in the shear profiles as functions of the radial coordinate for late times and early times respectively. It is clear that the perturbations to the shear close to the core are enhanced as the anisotropy increases. An increase in the perturbation to the shear is likely to result in greater internal friction between adjacent layers of stellar fluid and

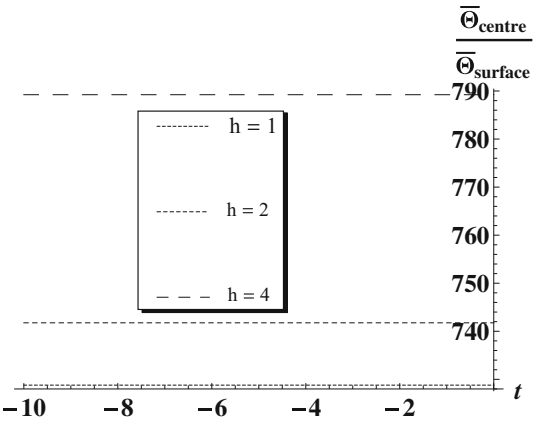

Fig. 19 Profiles of the ratio of collapse at the centre to the collapse rate at the surface versus time ($M = 1$ and $R = 6.6$)

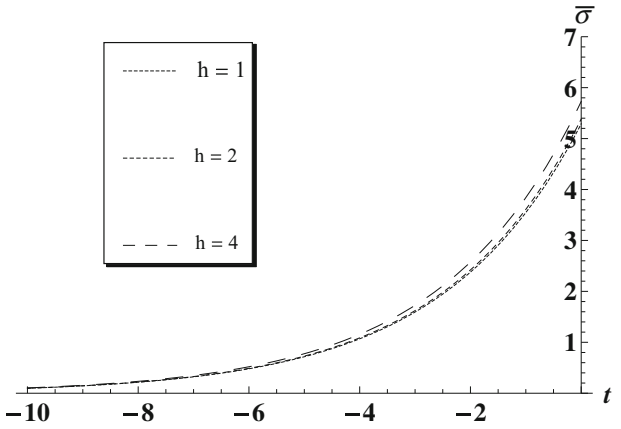

Fig. 20 Profiles of perturbed shear at the centre versus time ($M = 1$, $R = 6.6$ and $r = 0.01$)

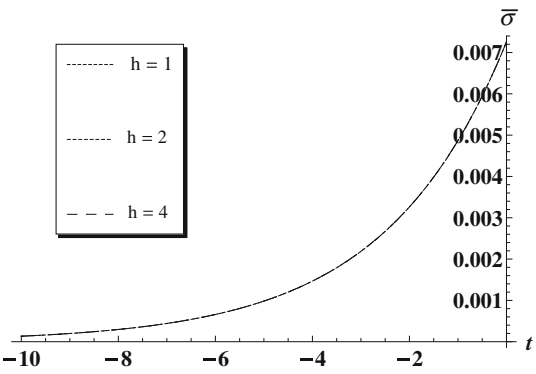

Fig. 21 Profiles of perturbed shear at the surface versus time ($M = 1$, $R = 6.6$ and $r = 0.01$)

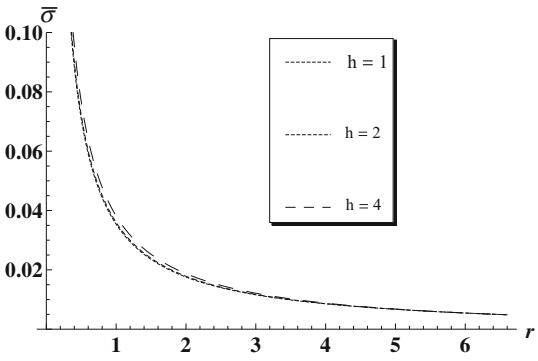

Fig. 22 Profiles of perturbed shear for late time collapse versus radial coordinate ($M = 1$, $R = 6.6$ and $t = -1$)

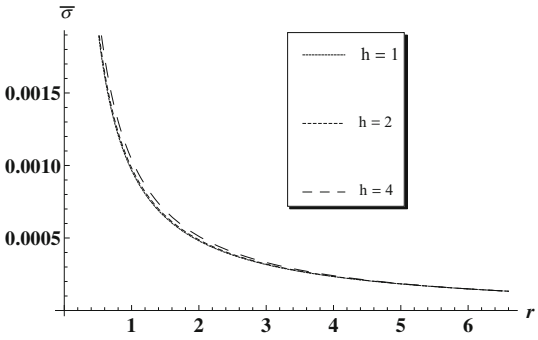

Fig. 23 Profiles of perturbed shear for early time collapse versus radial coordinate ($M = 1$, $R = 6.6$ and $t = -10$)

this mechanism is expected to enhance the temperature and heat flow near the core region.

8 Thermal behaviour

The importance of relaxational effects during dissipative gravitational collapse has been highlighted by several researchers. Govender and co-workers have shown that relaxational effects can lead to higher core temperatures and enhanced cooling at the surface of the collapsing body [19,41,48–50]. In order to explore the contributions from relaxational effects as the fluid exits from hydrostatic equilibrium we will employ a causal heat transport equation of Maxwell–Cattaneo form [51]. The truncated causal transport equation in the absence of rotation and viscous-heat coupling is given by

$$\tau_r h_a{}^b \dot{q}_b + q_a = -\kappa \left(h_a{}^b \nabla_b \mathcal{T} + \mathcal{T} \dot{u}_a \right), \tag{72}$$

where $h_{ab} = g_{ab} + u_a u_b$ is the projection tensor, $\mathcal{T}(t, r)$ is the local equilibrium temperature, $\kappa (\geq 0)$ is the thermal conductivity, and $\tau_r (\geq 0)$ is the relaxation time-scale over which causal, stable behaviour is achieved. The noncausal Fourier heat

transport equation is obtained by setting the relaxation time $\tau_r = 0$ in (72). With the aid of the metric (1), Eq. (72) becomes

$$\tau_r(qB)^{\cdot} + A(qB) = -\kappa\frac{(A\mathcal{T})'}{B}. \tag{73}$$

The thermodynamic coefficients associated with radiative transfer are well motivated in [19,20,34]. In order to obtain the casual temperature profile from (73) we take

$$\kappa = \gamma\mathcal{T}^3\tau_c, \quad \tau_c = \left(\frac{\xi}{\gamma}\right)\mathcal{T}^{-\omega}, \tag{74}$$

where τ_c is the mean collision time, ξ, γ and ω are positive constants. The relaxation time is taken to be of the order of the mean collision time

$$\tau_r = \left(\frac{\psi\gamma}{\xi}\right)\tau_c, \tag{75}$$

where ψ (≥ 0) is a constant. Employing the definitions for τ_r and κ, it can be shown that Eq. (73) takes the form

$$\psi(qB)^{\cdot}\mathcal{T}^{-\omega} + A(qB) = -\xi\frac{\mathcal{T}^{3-\omega}(A\mathcal{T})'}{B}, \tag{76}$$

where ψ can be considered to be a 'causality index', that enables us to quantify the impact of relaxation effects on the system. The noncausal case is obtained when $\psi = 0$. We now perturb the temperature as follows

$$\mathcal{T} = \mathcal{T}_o + \lambda\overline{\mathcal{T}}T, \tag{77}$$

where $\mathcal{T}_o$ is the equilibrium temperature. Using (77) and (76) (for the case of constant collision time i.e. $\omega = 0$), we obtain the following expression for the perturbed temperature

$$\begin{aligned}\overline{\mathcal{T}}(r) = &-\frac{2\psi}{\xi A_o}\frac{\ddot{T}}{T}\int\frac{1}{A_o}\mathcal{T}_o{}^{-3}\left[\left(\frac{y}{Y_o}\right)' - \frac{bY_o'}{B_oY_o} - \frac{y}{Y_o}\left(\frac{A_o'}{A_o} - \frac{Y_o'}{Y_o}\right)\right]dr\\ &-\frac{2}{\xi A_o}\frac{\dot{T}}{T}\int A_o\mathcal{T}_o{}^{\sigma-3}\left[\left(\frac{y}{Y_o}\right)' - \frac{bY_o'}{B_oY_o} - \frac{y}{Y_o}\left(\frac{A_o'}{A_o} - \frac{Y_o'}{Y_o}\right)\right]dr\\ &-\frac{a\mathcal{T}_o}{A_o} + \frac{C_1}{A_o},\end{aligned} \tag{78}$$

where C_1 is an integration constant. Relation (78) is a generalisation of the temperature perturbation obtained by Maharaj et al. [26] in which they investigated the collapse of a shear-free distribution of matter. The zeroth order perturbation of (76) yields

$$\mathcal{T}_o' = -\frac{A_o'}{A_o}\mathcal{T}_o, \tag{79}$$

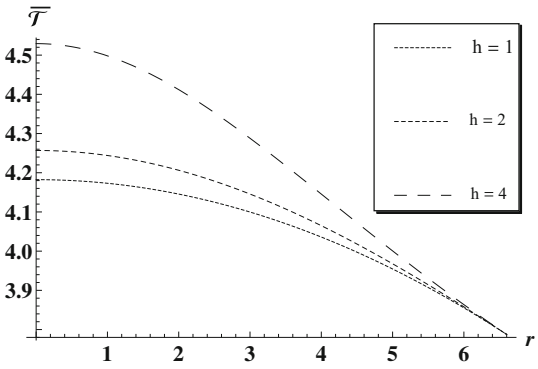

Fig. 24 Profiles of perturbed non-causal temperature $\overline{\mathcal{T}}$ versus radial coordinate ($M = 1$, $R = 6.6$, $C_o = 10$, $C_1 = \sqrt{10}$, $\xi = 100$, $\psi = 0$)

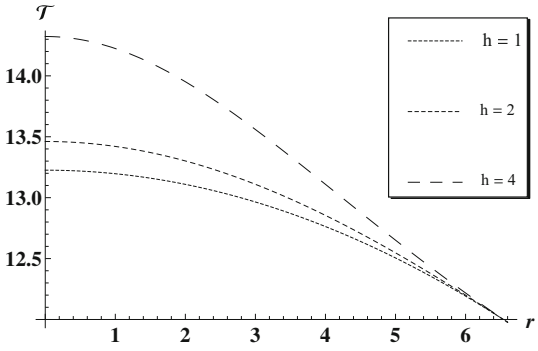

Fig. 25 Profiles of total non-causal temperature $\mathcal{T}$ versus radial coordinate ($M = 1$, $R = 6.6$, $C_o = 10$, $C_1 = \sqrt{10}$, $\xi = 100$, $\psi = 0$ and $\lambda = 0.001$)

which can be easily expressed as

$$\left(A_o \mathcal{T}_o\right)' = 0. \tag{80}$$

Equation (80) easily integrates to give

$$\mathcal{T}_o = \frac{C_o}{A_o}, \tag{81}$$

where C_o is a positive constant of integration. Herrera and Santos [52] and Maharaj et al. [26] privide a discussion of the physical significance of Eq. (79), which was first obtained by Tolman in 1930. They point out that Eq. (79) alludes to the existence of a temperature gradient which prohibits the movement of heat flux along the gradient of the gravitational field. This mechanism is responsible for the thermal equilibrium being maintained in the presence of a gravitational field.

From Fig. 24 we note that the perturbations in the temperature are greatest when there is a greater divergence from isotropy with p_r dominating p_t. This is in keeping with a greater generation of heat within the core due to internal friction between the neighbouring layers of the stellar fluid. Figure 25 shows that anisotropy leads to higher core temperatures with the effect being dominant near the central regions of the

collapsing body. An interesting and surprising result is that the causal and noncausal temperatures are identical for this particular epoch of the collapse which is markedly different from the shear–free case with isotropic pressure [26]. Bearing in mind that the isotropic model corresponds to $h = 1$ for which we obtain identical profiles for the perturbations in the causal and noncausal temperatures, it follows that relaxational effects are sensitive to the presence of shear $\left(\frac{b}{B_o} \neq \frac{y}{Y_o}\right)$ which can be further enhanced by density inhomogeneities and heat flow [28].

9 Conclusion

We have investigated the impact of anisotropy on the physical behaviour of a spherically symmetric stellar fluid undergoing shearing dissipative collapse. Our system is initially static and is then subjected to linear perturbations that drive the system away from hydrostatic equilibrium. The initial static core is described by the Bowers and Liang model which is the anisotropic generalisation of the Schwarzschild uniform density sphere. The effect of pressure anisotropy on the collapse process is clearly evidenced on the perturbations to the energy density, radial pressure, tangential pressure, heat flow, collapse rate and shear. We have shown that the perturbations are enhanced with growing anisotropy. An interesting finding in our work is that the perturbations to the temperature profiles in both the Eckart and noncausal regimes are identical. This is in contrast to the shear-free, isotropic models studied in [26]. We must point out that the causal temperature perturbations were obtained by using a truncated heat transport equation of Maxwell–Cattaneo form. It would be interesting to investigate the evolution of these perturbations by invoking the full causal heat transport equation.

Acknowledgments The authors are grateful to the referees for useful and constructive comments which helped clarify the main results of the paper. We also thank Professor Luis Herrera (Escuela de Fisica, Facultad de Ciencias, Universidad Central de Venezuela) for insightful advice and suggestions in finalising this manuscript. MG and SDM thank the National Research Foundation and the University of KwaZulu Natal for financial support. SDM further acknowledges that this research is supported by the South African Research Chair Initiative of the Department of Science and Technology. KPR wishes to thank the Directorate for Research and Postgraduate Support at the Durban University of Technology, in particular Prof. S. Moyo, for a lecturer replacement grant which helped make this study possible.

References

1. Vaidya, P.C.: Proc. Indian Acad. Sci. A **33**, 264 (1951)
2. Santos, N.O.: Mon. Not. R. Astron. Soc. **216**, 403 (1985)
3. De Oliveira, A.K.G., Santos, N.O.: Astrophys. J. **312**, 640 (1987)
4. Herrera, L., Le Denmat, G., Santos, N.O.: Mon. Not. R. Astron. Soc. **237**, 257 (1989)
5. Chan, R., Herrera, L., Santos, N.O.: Mon. Not. R. Astron. Soc. **267**, 637 (1994)
6. Chan, R.: Astron. Astrophys. **368**, 325 (2001)
7. Di Prisco, A., Herrera, L., Le Denmat, G., MacCallum, M.A.H., Santos, N.O.: Phys. Rev. D **76**, 064017 (2007)
8. Eckart, C.: Phys. Rev. **58**, 919 (1940)
9. Israel, W.: Ann. Phys. NY **100**, 310 (1976)
10. Israel, W., Stewart, J.: Phys. Lett. A **58**, 213 (1976)
11. Israel, W., Stewart, J.: Ann. Phys. NY **118**, 341 (1979)

12. Pavón, D., Jou, D., Casas-Vázquez, J.: Ann. Inst. H Poicaré **A36**, 79 (1982)
13. Cattaneo, C.: Atti. Semin. Mat. Fis. Univ. Modena **3**, 3 (1948)
14. Di Prisco, A., Herrera, L., Esculpi, M.: Class. Quantum Grav. **13**, 1053 (1996)
15. Anile, A.M., Pavon, D., Romano, V.: The Case for Hyperbolic Theories of Dissipation in Relativistic Fluids. arXiv:gr-qc/9810014
16. Herrera, L., Martínez, J.: Gen. Relativ. Gravit. **30**, 445 (1998)
17. Di Prisco, A., Herrera, L., Esculpi, M.: Class. Quantum Grav. **13**, 1053 (1996)
18. Di Prisco, A., Herrera, L., Falcon, N., Esculpi, M., Santos, N.O.: Gen. Relativ. Gravit. **29**, 1391 (1997)
19. Govender, M., Maharaj, S.D., Maartens, R.: Class. Quantum Grav. **15**, 323 (1998)
20. Govender, M., Maartens, R., Maharaj, S.D.: Mon. Not. R. Astron. Soc. **310**, 557 (1999)
21. Govinder, K.S., Govender, M.: Phys. Lett. A **283**, 71 (2001)
22. Govender, M., Govinder, K.S.: Int. J. Theor. Phys. **41**, 1797 (2002)
23. Naidu, N.F., Govender, M.: J. Astrophys. Astr. **28**, 167 (2007)
24. Naidu, N.F., Govender, M., Govinder, K.S.: Int. J. Mod. Phys. D **15**, 1053 (2006)
25. Rajah, S.S., Maharaj, S.D.: J. Math. Phys. **49**, 012501 (2008)
26. Maharaj, S.D., Govender, G., Govender, M.: Pramana Phys. **77**, 469 (2011)
27. Thirukkanesh, S., Rajah, S.S., Maharaj, S.D.: J. Math. Phys. **53**, 032506 (2012)
28. Govender, M., Reddy, K.P., Maharaj, S.D.: Int. J. Mod. Phys. D **02**, 1450013 (2014)
29. Ruderman, M.: Ann. Rev. Astron. Astrophys. **10**, 427 (1972)
30. Cameron, A.G.W., Canuto, V.: In: Proceedings of the 16th Solvay Conference on Astrophysics and Gravitation: Neutron Stars: General Review, de l'Université de Bruxelles, Bruxelles (1973)
31. Uslov, V.V.: Phys. Rev. D **70**, 067301 (2004)
32. Weber, F.: Pulsars as Astrophysical Observatories for Nuclear and Partcile Physics. IOP Publishing, Bristol (1999)
33. Herrera, L., Santos, N.O.: Phys. Rep. **286**, 53 (1997)
34. Martinez, J.: Phys. Rev. D **53**, 6921 (1996)
35. Bowers, R.L., Liang, E.P.T.: Astrophys. J. **188**, 657 (1974)
36. Dev, K., Gleiser, M.: Gen. Relativ. Gravit. **34**, 1793 (2002)
37. Dev, K., Gleiser, M.: Gen. Relativ. Gravit. **35**, 1435 (2003)
38. Chan, R.: Astrophys. Space Sci. **206**, 219 (1993)
39. Herrera, L.: Int. J. Mod. Phys. D **20**, 1689 (2011)
40. Sharma, R., Das, S.: J. Gravit. **2103**, 659605 (2013)
41. Govender, G., Govender, M., Govinder, K.S.: Int. J. Mod. Phys. D **19**, 1773 (2010)
42. Govender, M., Govinder, K.S., Fleming, D.: Int. J. Theor. Phys. **51**, 3399 (2012)
43. Herrera, L., Di Prisco, A., Ospino, J.: Gen. Relativ. Gravit. **42**, 1585 (2010)
44. Chan, R., Herrera, L., Santos, N.O.: Mon. Not. R. Astron. Soc. **265**, 533 (1993)
45. Chan, R., Kichenassamy, S., Le Denmat, G., Santos, N.O.: Mon. Not. R. Astron. Soc. **239**, 91 (1989)
46. Herrera, L., Le Denmat, G., Santos, N.O.: Gen. Relativ. Gravit. **44**, 1143 (2012)
47. Florides, P.S.: Proc. R. Soc. Lond. A. **337**, 529 (1974)
48. Govender, M., Govinder, K.S., Maharaj, S.D., Sharma, R., Mukherjee, S., Dey, T.K.: Int. J. Mod. Phys. D **12**, 667 (2003)
49. Govinder, K.S., Govender, M.: Gen. Relativ. Gravit. **44**, 147 (2012)
50. Govender, M.: Int. J. Mod. Phys. D **22**, 1350049 (2013)
51. Maartens, R.: Causal Thermodynamics in Relativity. arXiv:astro-ph/9609119
52. Herrera, L., Santos, N.O.: Mon. Not. R. Astron. Soc. **287**, 161 (1997)